Ice pumping: ice thickness gradients steer the Arctic Ocean Circulation

Gianluca Meneghello[a,b] , Michael A. Spall[b]

[a] *Ecole normale supérieure, Université PSL, Paris, France*
[b] *Woods Hole Oceanographic Institution, Woods Hole, MA*

ABSTRACT: Surface currents beneath sea ice are constrained by ice thickness in much the same way bottom currents are constrained by bathymetry. Despite the gentle slope of the ice cover—only a few meters over thousands of kilometers—surface currents on the order of a few centimeters per second generate vertical velocities of a few meter per year, which is the same order of magnitude as the surface Ekman pumping. We dub this vertical velocity "ice pumping". Using theory and numerical modeling, we show that this ice pumping exerts a first-order control on both the structure and intensity of the large-scale Arctic Ocean circulation. The dominant effect is the generation of a basin-scale anticyclonic circulation anomaly, forced by the interaction of the Transpolar Drift Current with the overlying sea-ice growing thicker towards Greenland. The most notable consequence is a shift of the Transpolar Drift Current itself towards the Eurasian coast, and a modulation of the intensity of the large-scale circulation. Ice pumping should therefore be considered alongside Ekman pumping, mesoscale eddies and the ice–ocean governor as a fundamental constraint on Arctic circulation, and is likely to be important in other scenarios, such as ice-covered exoplanets.

1. Introduction

This paper examines how ice-thickness gradients can steer the large-scale circulation of the Arctic Ocean. Unlike mid-latitude basins, meridional gradients of planetary vorticity in the central Arctic are weak and cannot offset the Ekman-driven input of vorticity into the water column. A classical Sverdrup balance (Sverdrup 1947; Munk 1950) would therefore imply currents much stronger than the observed ones, making it necessary to account for additional mechanisms.

Two such mechanisms have been suggested over the past decade. The first is the advection of potential vorticity by the mean flow (Spall 2020) and by eddy fluxes (Davis et al. 2014; Lique et al. 2015; Manucharyan and Spall 2015; Yang et al. 2016; Meneghello et al. 2017). Mean advection matters when the forcing is asymmetric. Eddy fluxes — generated by baroclinic instability — tend to relax the potential vorticity gradients generated by wind- and ice-driven Ekman pumping.

The second mechanism, dubbed the ice-ocean governor, involves the interaction between ice drift and surface currents (Meneghello et al. 2018a,b, 2020; Dewey et al. 2018; Zhong et al. 2018). As the surface-current velocity approaches the ice-drift velocity, surface stresses and Ekman pumping are reduced, and the potential vorticity input can in theory be driven to zero, thereby alleviating the need for potential vorticity advection. Subsequent theoretical (Doddridge et al. 2019) and observational (Meneghello et al. 2020) studies have shown that both mean/eddy advection and the ice–ocean governor contribute to the equilibration of the Arctic circulation, albeit on different time scales.

Corresponding author: Gianluca Meneghello, gianluca.meneghello@lmd.ipsl.fr

An additional constraint on the large-scale circulation in high-latitude oceans is bathymetry. In the absence of strong planetary vorticity gradients, the barotropic component of the flow tends to follow bathymetric contours to conserve potential vorticity. Although this steering weakens as the flow becomes increasingly baroclinic on long time scales, bathymetry can still influence long-term mean currents (Nöst and Isachsen 2003), and remotely forced deep flows may exert a similar steering effect on the surface circulation (Nilsson et al. 2024). In the present work, however, our focus is on mechanisms that operate independently of topographic control, and we therefore neglect bathymetric effects.

We focus instead our attention on an additional constraint on high-latitude circulation: variations in ice thickness. In this framework, summarized in Figure 1, ice thickness acts as an upside-down bathymetry and steers the currents away from the pathways they would otherwise follow in the absence of ice-thickness gradients. Although ice-cover slopes are two to three orders of magnitude smaller than bathymetric slopes, surface currents are often much stronger than their deep counterparts, making their interaction non-negligible. Most importantly, this upside-down bathymetry interacts with both barotropic and baroclinic components and therefore remains relevant even on the long time scales over which deep currents are expected to be weak.

Our discussion is organized as follows. Section 2 introduces a dynamical balance that includes Ekman pumping, the advection of planetary vorticity, eddy fluxes, the ice–ocean governor, and the ice pumping associated with the upside-down bathymetry. We provide observational and theoretical estimates of the role played by each process. We focus on the equilibrated state, assume that deep

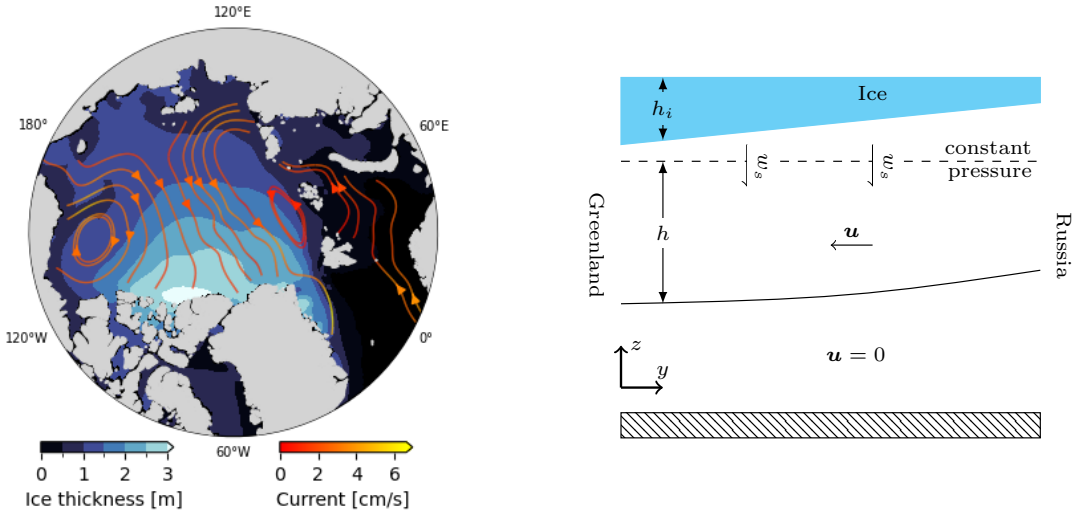

(a) (b)

FIG. 1: (a): Ocean currents (streamlines) flowing beneath a sloped sea-ice cover (contours) induce an ice-pumping effect analogous to Ekman pumping, locally squeezing or stretching the underlying water column. (b): Schematic representation of ice pumping, illustrating the conceptual model used in this study. Ocean currents are derived from dynamic ocean topography (Armitage et al. 2016, 2017), while the sea-ice thickness dataset is described by Ricker et al. (2017). Datasets are restricted to the cold-season period (15 October–15 April) and averaged over 2011–2020, reflecting the availability of sea-ice thickness observations.

currents are at rest, and use a simple thickness-diffusion parameterization to represent mesoscale turbulence. We relax several of these assumptions in Section 3, where we examine the role of ice pumping using a shallow-water numerical model. Such a model allows us to include a non-parameterized eddy field, barotropic and first baroclinic modes, and a time-varying forcing. We conclude in Section 4 with a discussion of the implications for the Arctic circulation in particular and for ice-covered oceans more generally.

2. The role of ice pumping in driving the large scale circulation

a. Dynamical balance

Our analysis starts with the geostrophic relations and vertically-integrated continuity equation (including an eddy thickness flux divergence) for the 1.5 layer model shown in Figure 1b:

$$u = -\frac{g'}{f}\frac{\partial h}{\partial y} \qquad v = \frac{g'}{f}\frac{\partial h}{\partial x} \tag{1a}$$

$$\nabla\cdot(\boldsymbol{u}h + \overline{\boldsymbol{u}'h'}) = w_s \tag{1b}$$

where h is the layer thickness, $\boldsymbol{u} = (u, v)$ the time-averaged geostrophic velocity, $\overline{\boldsymbol{u}'h'}$ the thickness flux due to eddies, g' is the reduced gravity and w_s the vertical velocity at a constant pressure depth below the well mixed surface layer, as shown in Figure 1b. We here neglect the bathymetry-induced vertical velocity at the ocean floor, consistently with the assumption that the bottom layer is at rest. It is also assumed that the flow is adiabatic so there is no mass exchange between the upper layer and the deep layer. A constant layer thickness h is imposed as a boundary condition to enforce no normal flow.

Substitution of the geostrophic relations into the continuity equation, and assuming a parameterization of the eddy fluxes $\overline{\boldsymbol{u}'h'} = -K\nabla h$ with K a constant diffusivity, we obtain

$$\underbrace{\frac{g'}{2f^2}J(h^2, f)}_{\text{Planetary vorticity advection}} - \underbrace{K\nabla^2 h}_{\text{Thickness diffusion}} = w_s \tag{2}$$

The first term represent the advection of planetary vorticity, the second term is the parameterized thickness diffusion. $J(a,b) = \left(\hat{\mathbf{k}}\times\nabla a\right)\cdot\nabla b = \frac{\partial a}{\partial x}\frac{\partial b}{\partial y} - \frac{\partial a}{\partial y}\frac{\partial b}{\partial x}$ is the Jacobian.

The vertical velocity w_s includes both an Ekman pumping component and an ice pumping component, the latter

driven by currents flowing under the sloping sea ice cover,

$$w_s = \underbrace{\nabla \times \frac{\boldsymbol{\tau}}{\rho f}}_{\text{Ekman pumping}} - \underbrace{\boldsymbol{u} \cdot \nabla h_i}_{\text{Ice pumping}} \tag{3}$$

where τ is the stress at the ocean surface and ∇h_i is the ice thickness gradient. Ice pumping is downward if the velocity is in the direction of the ice thickness gradient, as in Figure 1.

Under the assumptions that (i) the surface stress is linear in the wind and ice–ocean relative velocity, $\boldsymbol{\tau} = (1-\alpha)C_a\rho_a\boldsymbol{u}_a + \alpha C_i\rho(\boldsymbol{u}_i - \boldsymbol{u})$, where α is the ice concentration (ii) gradients of the ice concentrations are negligible in the Ekman pumping computations, $\nabla \times (\alpha \boldsymbol{u}) \approx \alpha \nabla \times \boldsymbol{u}$; (iii) variations of the Coriolis parameter f are negligible in all terms except the planetary vorticity advection; and (iv) $\boldsymbol{u}$ is the geostrophic velocity given by (1a), so that vorticity can be expressed as $\nabla \times \boldsymbol{u} = (g'/f_0)\nabla^2 h$, the dynamical balance (2) can be formulated in terms of the layer thickness h:

$$\underbrace{\frac{g'}{2f_0^2} J\left(h^2, f\right)}_{\text{Planetary vorticity advection}} - \underbrace{K\nabla^2 h}_{\text{Thickness diffusion}} = \underbrace{(1-\alpha)w_a + \alpha w_i}_{\text{Ekman pumping before accounting for ice–ocean feedback}} - \underbrace{\alpha \frac{C_i g'}{f_0^2}\nabla^2 h}_{\text{Ice-ocean governor}} + \underbrace{\frac{g'}{f_0} J\left(h, h_i\right)}_{\text{Ice pumping}} \tag{4}$$

where $w_a = \frac{C_a}{f_0}\frac{\rho_a}{\rho}\nabla \times \boldsymbol{u}_a$ and $w_i = \frac{C_i}{f_0}\nabla \times \boldsymbol{u}_i$ are the prescribed wind- and ice-driven Ekman pumpings before accounting for any ice–ocean feedback.

It is worth noting that, under the β-plane approximation, the first term on the left-hand side reduces to the classical Sverdrup term $\frac{g'\beta_0}{2f_0^2}\frac{\partial h^2}{\partial x}$. In polar regions, however, the β-plane approximation does not hold, and a higher-order expansion of the gradient of the Coriolis parameter is required:

$$f(s) \approx f_0 + \beta_0 s + \frac{\gamma_0}{2} s^2 \tag{5}$$

where $\beta_0 = \frac{\partial f}{\partial s}$ and $\gamma_0 = \frac{\partial^2 f}{\partial s^2}$ and $s = \sqrt{x^2 + y^2}$ is the distance from the North Pole.

b. Dimensional analysis

Insights on the role of the different processes in the balance (4) can be obtained by making the equation dimensionless after defining a characteristic vertical length scale H, horizontal length scale L, geostrophic velocity scale U and an Ekman pumping scale W. We furthermore denote the characteristic ice-thickness scale as H_i. Note that these choices reflect basin-scale balances, not smaller scale gyres or boundary currents. The dimensionless balance can be rewritten as

$$\underbrace{\mathsf{B}\,\tilde{J}(\tilde{h}^2, \tilde{f})}_{\text{Planetarty vorticity advection}} + \underbrace{(\alpha\mathsf{G} + \mathsf{K})\,\tilde{\nabla}^2\tilde{h}}_{\text{Ice-ocean governor thickness diffusion}} - \underbrace{\mathsf{P}\,\tilde{J}(\tilde{h}, \tilde{h}_i)}_{\text{Ice pumping}} = \underbrace{(1-\alpha)\tilde{w}_a + \alpha\tilde{w}_i}_{\text{Ekman pumping before accounting for ice–ocean feedback}} \tag{6}$$

The dimensionless parameters B, K, G, and P, defined in Table 1, quantify the relative roles of planetary-vorticity advection, eddy fluxes, ice–ocean coupling, and ice pumping. In the Arctic, all of them take characteristic values of order 1. The right-hand side involves only the prescribed Ekman pumping terms $\tilde{w}_a = \frac{w_a}{W}$ and $\tilde{w}_i = \frac{w_i}{W}$ weighted by the ice concentration α and nondimensionalized by the velocity scale W. Tildes denote dimensionless variables and operators, and $\tilde{f} = \frac{f}{f_0}$.

Estimates for each of these terms based on observations and reanalysis over the Arctic demonstrate their approximate magnitudes and patterns (Fig. 2). The Ekman pumping and ice-ocean governor terms are the largest, especially in the Beaufort Gyre, but they also largely cancel so that their net effect is much smaller. Planetary vorticity advection is similarly large in the Beaufort Gyre, reflecting the anticyclonic circulation there. Thickness diffusion is upward in the gyre region as a result of the export of low potential vorticity eddies from the gyre, and weak over much of the central Arctic. Ice pumping is smaller than these other terms, but is negative over the entire Arctic interior, indicating its importance for the large-scale circulation.

It is worth remarking how both the eddy fluxes and the ice-ocean governor parameters, K and G, multiply a Laplacian, despite representing very different physical processes: a parameterized thickness diffusion by mesoscale turbulence for eddy fluxes, and the vorticity of the surface geostrophic current for the ice-ocean governor.

c. Dynamical balances of the Arctic Ocean circulation

To understand the interplay among the different processes, it is instructive to solve (6) under several different limits. We start by investigating the balance between Ekman pumping and i) planetary-vorticity advection ($\mathsf{B} = 1$), ii) governor/eddy fluxes ($\alpha\mathsf{G} + \mathsf{K} = 1$) and iii) ice pumping ($\mathsf{P} = 1$). The remaining parameters for each configuration

Symbol	Expression	Value	Units	Description
f_0	–	1.45×10^{-4}	s^{-1}	Coriolis parameter
β_0	–	0	$m^{-1}s^{-1}$	Meridional gradient of Coriolis parameter
a	–	6.4×10^{6}	m	Earth's radius
γ_0	f_0/a^2	3.5×10^{-18}	$m^{-2}s^{-1}$	Second derivative of Coriolis parameter (γ plane approx.)
H	–	100	m	Characteristic layer thickness anomaly
H_i	–	1	m	Characteristic ice thickness anomaly
L	–	1×10^{6}	m	Characteristic horizontal length
K	–	300	m^2s^{-1}	Eddy diffusivity
C_i	–	5×10^{-4}	$m\,s^{-1}$	Drag velocity (dimensional)
U_i	–	2×10^{-2}	$m\,s^{-1}$	Ice velocity
g'	$\frac{g\Delta\rho}{\rho}$	2.5×10^{-2}	$m\,s^{-2}$	Reduced gravity
U	$\frac{g'}{f_0}\frac{H}{L}$	2×10^{-2}	$m\,s^{-1}$	Geostrophic velocity
W	$\frac{C_i}{f_0}\frac{U_i}{L}$	1×10^{-7}	$m\,s^{-1}$	Ekman pumping velocity
B	$\frac{U}{W}\frac{H}{L}\frac{\gamma_0 L^2}{2f_0}$	0.30	–	Non-dimensional planetary vorticity parameter
G	$\frac{U}{W}\frac{C_i}{f_0 L}$	0.86	–	Non-dimensional ice-ocean governor parameter
P	$\frac{U}{W}\frac{H_i}{L}$	0.25	–	Non-dimensional ice pumping parameter
K	$\frac{K}{W}\frac{H}{L^2}$	0.43	–	Non-dimensional eddy diffusivity parameter

TABLE 1: Parameters and Arctic reference values.

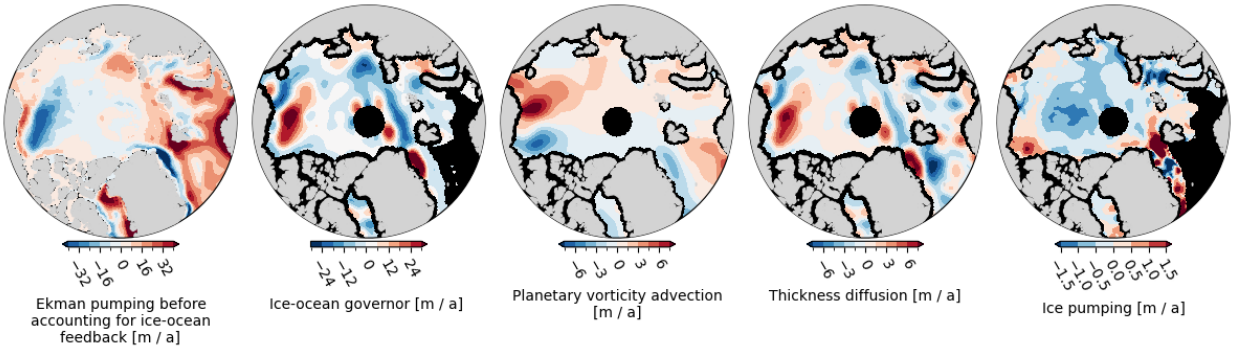

FIG. 2: Observational estimates of the individual contributions to the vorticity balance, as defined in equation (4). The values of the parameters are taken from Table 1. The observational datasets used in this estimate are: sea-ice thickness from Ricker et al. (2017); sea-ice concentration from Meier et al. (2024); sea-ice velocity from Tschudi et al. (2019); dynamic ocean topography from Armitage et al. (2016, 2017); and geostrophic winds derived from atmospheric geopotential fields from Hersbach et al. (2023). Datasets are restricted to the cold-season period (15 October–15 April) and averaged over 2011–2020, reflecting the availability of sea-ice thickness observations.

are set to zero, with the exception of the eddy fluxes and the ice–ocean governor parameters that are set to a minimum of $\alpha\mathsf{G}+\mathsf{K}=10^{-3}$ solely for numerical stability. The imposed Ekman-pumping field, ice thickness, and Coriolis parameter distribution, common to all configurations, are shown in Figure 3. A Dirichlet boundary condition $\tilde{h}_b=1$ is imposed to enforce no normal flow at the boundary, with the exception of case i) where $\tilde{h}_b$ is increased to 3 to prevent outcropping. The resulting circulations, as inferred from the layer thickness (streamfunction), are shown in Figure 4.

Potential-vorticity conservation considerations dictates the circulation, and the computed currents differs both in direction and in magnitude. When planetary vorticity advection is the only balance to Ekman pumping, as in Figure 4a, the flow outside the Ekman-pumping region follows f-contours. Within regions of Ekman pumping, upwelling stretches the water column and drives the circulation poleward — toward larger f, so that f/h is conserved — while downwelling compresses the column and drives it equatorward toward smaller f. The Transpolar Drift Current flows from the upwelling region on the right to the downwelling region to the left. The transport is large: potential vorticity

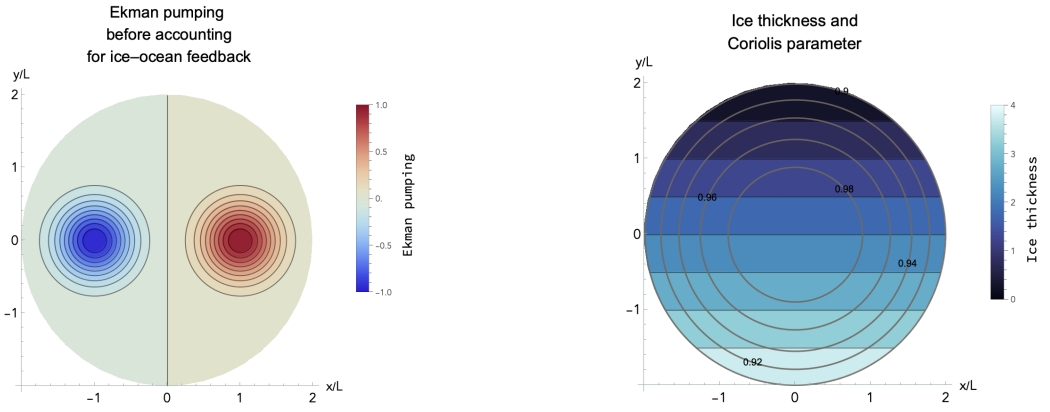

(a) (b)

FIG. 3: The model setup. (a) Ekman pumping prior to the inclusion of ice–ocean feedback; (b) ice thickness (color) and dimensionless Coriolis parameter f/f_0 (contours).

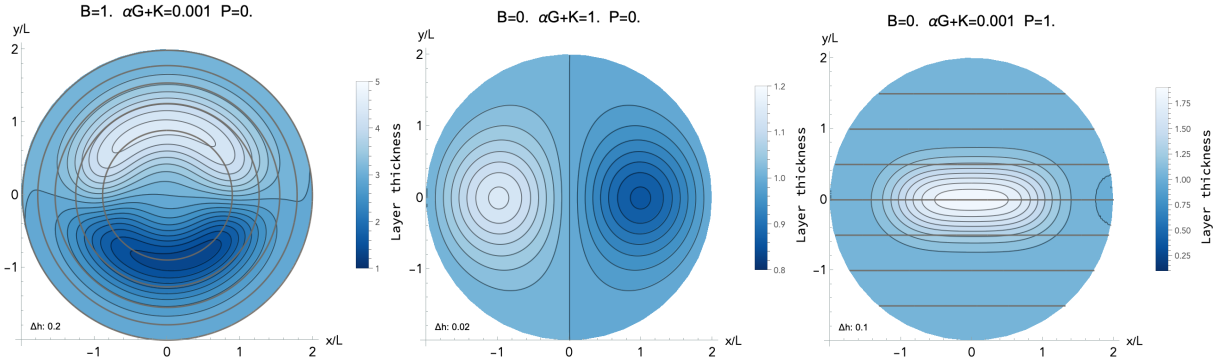

(a) (b) (c)

FIG. 4: (a) The planetary-vorticity-balanced circulation—equivalent to the Sverdrup balance at lower latitudes; (b) The governor/thickness-diffusion balanced circulation; (c) the ice-pumping-balanced circulation. The layer thickness contour interval Δh, indicated in the bottom left corner of each panel, varies across panels. Thick gray contours mark lines of constant Coriolis parameter in (a) and constant ice thickness in (c), same as Figure 3b.

is advected solely by the mean flow, which is confined to a relatively narrow and intense current flowing across the pole. Counterintuitively, the shallower and deeper layer thicknesses are found where the Ekman pumping is zero rather than in proximity of the maximum upwelling and downwelling. The planetary-vorticity balanced flow is nearly perpendicular to the observed Arctic circulation, highlighting the importance of the other terms in the potential vorticity balance. A similar circulation pattern was found by Willmott and Luneva (2015) for a barotropic polar plane.

The eddy and ice-ocean governor balanced circulation is shown in Figure 4b. Eddies flux potential vorticity between the downwelling region and the upwelling region, and the mean flow merely reflects the requirement for an isopycnal slope to sustain these eddy fluxes. In contrast, the ice-ocean governor reduces the Ekman pumping, and the mean flow reflect the surface currents catching up with the ice drift and limiting the surface stress. In both regimes, the mean flow does not transport net potential-vorticity between upwelling and downwelling regions, and the flow is substantially weaker. Two counter-rotating gyres develop, matching the imposed Ekman pumping pattern and canceling its effect.

Laslty, the ice-pumping balanced circulation is shown in Figure 4c. Outside Ekman-pumping regions, the current is forced to follow ice-thickness contours to conserve potential vorticity, and is thus blocked when these intersect the boundary. Within the forcing region, Ekman upwelling drives the circulation toward thicker ice at the bottom of

the figure, generating a compensating ice-pumping downwelling, and vice-versa. The combined effect is a single anticyclonic gyre spanning the entire area between the two Ekman pumping regions. As for the ice-ocean governor, the current flowing beneath the sloping sea ice cover cancels the Ekman pumping and the net transport of potential vorticity between the upwelling and downwelling regions is zero.

How does ice pumping reshape the circulation when all processes contribute to the balance? Figure 5 shows the circulation when planetary vorticity advection and governor/eddy fluxes, but no ice-pumping are active (B = 1, αG + K = 1, P = 0) (a) and when all three processes are active (B = 1, αG + K = 1, P = 1) (b). The introduction of the ice pumping modifies the circulation by shifting and deflecting the Transpolar Drift Current towards the Eurasian coast on the right. Its net effect, shown in Figure 5c, is an anticyclonic circulation whose transport per unit depth $\tilde{T} = \max(\tilde{h}) - \tilde{h}_b \approx 0.1$, where $\tilde{h}_b$ is the thickness boundary value, is comparable to the $\tilde{T} \approx 0.2$ transport of the two original gyres.

3. Numerical experiments

The basic influences of ice cover slopes predicted by the theory in Section 2 are now evaluated with the use of an idealized numerical model. The model solves the two-layer shallow water equations in a circular domain with a pole at its center. The model is forced by a specified surface stress representing the stress imparted on the ocean by either wind or ice motion. The model includes physics not represented in the theory, including nonlinearities, explicit eddy fluxes, two active layers, and explicit closure of eddy fluxes at the boundaries. The influence of the ice-ocean interaction is demonstrated by adding a vertical velocity into layer 1 that represents the pumping/suction resulting from surface currents oriented along the ice cover slope.

a. Model formulation

The momentum equations are written as

$$\frac{\partial u_k}{\partial t} + (f+\zeta_k)v_k = -\frac{\partial (P_k + E_k)}{\partial x} - \delta_{k1}\frac{C_i u_k}{h_k} - \delta_{k2}\frac{C_d u_k}{h_k} + A\nabla^2 u_k \tag{7a}$$

$$\frac{\partial v_k}{\partial t} - (f+\zeta_k)u_k = -\frac{\partial (P_k + E_k)}{\partial y} + \delta_{k1}\frac{\tau^y}{\rho_0 h_k} - \delta_{k1}\frac{C_i v_k}{h_k} - \delta_{k2}\frac{C_d v_k}{h_k} + A\nabla^2 v_k \tag{7b}$$

where $k = 1,2$ is the layer, u and v are the horizontal velocities in the x and y directions, h is the layer thickness, τ^y is the stress in the y direction, $\zeta_k = \partial v_k/\partial x - \partial u_k/\partial y$ is the relative vorticity, $E_k = (u_k^2 + v_k^2)/2$ is the kinetic energy, $g' = (\rho_2 - \rho_1)g/\rho_2$ is the reduced gravity, and ρ_0 is a reference density. δ_{ij} is the Kroneker delta, which equals one when $i = j$ and zero otherwise. The Coriolis parameter varies with latitude as $f = 1.45 \times 10^{-4} \sin\theta$, where θ is latitude with the pole at the center of the domain. The model is forced by a stress in the y direction applied as a body force in layer 1. Dissipation is represented by a linear bottom drag in layer 2 (C_d), a linear ice-ocean drag in layer 1 (C_i), and a lateral Laplacian viscosity with no-slip boundary conditions. The viscosity coefficient A is dependent on the velocity strain and shear, following Smagorinsky (1963), as

$$A = (\nu_s/\pi)^2 \Delta^2 \left[\left(\frac{\partial u}{\partial x} - \frac{\partial v}{\partial y} \right)^2 + \left(\frac{\partial u}{\partial y} + \frac{\partial v}{\partial x} \right)^2 \right]^{1/2}. \tag{8}$$

There is no exchange of mass between layers in the continuity equation but there is a mass source term forced by the gradient in ice thickness added at the top of layer 1.

$$\frac{\partial h_k}{\partial t} + \nabla \cdot (h_k \boldsymbol{u}_k) = -(2-k)\boldsymbol{u}_1 \cdot \nabla h_i \tag{9}$$

The term on the right hand side is the vertical velocity resulting from the horizontal velocity interacting with the ice cover slope (only applied to layer 1). In this construct we can think of the surface of layer 1 as residing at the base of the ice at its thickest point. The vertical velocity through this surface represents the conservation of mass in the region between the ice and this surface. The top of layer 1 is also a surface of uniform pressure arising from the ice and water lying above it, so in that sense it is akin to a free surface in the absence of sea ice.

Finally, the pressure is calculated from the hydrostatic equation as

$$P_1 = g(h_1 + h_2) \qquad P_2 = P_1 - g' h_1. \tag{10}$$

The model domain is circular with radius $r_0 = 1000$ km and a flat bottom. The initial layer thicknesses are $h_1 = 200$ m and $h_2 = 400$ m with a reduced gravity between the two layers of $g' = 0.025$ m s^{-2}. The horizontal grid spacing is 5.5 km, which is less than the baroclinic deformation radius of 13 km, so the model resolves first mode baroclinic eddies well. The surface stress is independent of y and defined to represent two gyres separated by a flow in the negative y direction. This is a crude representation of the anticyclonic Canada Basin and cyclonic Eurasian Basin, separated by the Transpolar Drift Current directed from Russia towards Greenland (see Figure 1). The maximum surface stress is $\tau_0 = -0.015$ Nm^{-2}.

$$\tau^y = \tau_0 \cos(\pi(x - r_0)/r_0) \tag{11}$$

The depth of the sea ice is specified as a linear function of y, increasing from $h_{min} = 0.5$ m at $y = 2r_0$ km to $h_{max} = 5.5$ m at $y = 0$.

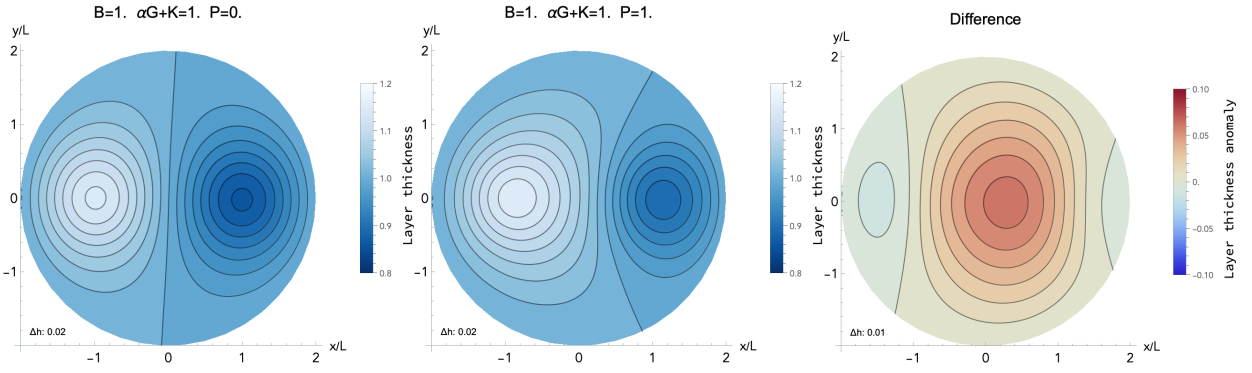

FIG. 5: The circulation with (a) and without (b) ice pumping. Planetary-vorticity advection and eddy-flux/ice–ocean-governor are given equal weight. The introduction of ice pumping generates an anomalous circulation between the two gyres driving a cross-gyres transport comparable to the transport of the original gyre (c). The contour interval Δh, indicated in the bottom left corner of each panel, varies across panels.

$$h_i = h_{min} + (h_{max} - h_{min})(2r_0 - y)(1 + \phi\cos(2\pi t/\Theta))/(1+\phi) \quad (12)$$

This is, of course, a gross simplification of the actual ice distribution, which varies in space and time. The term proportional to ϕ represents a simple seasonal cycle, where Θ is one year, although for our central calculation $\phi = 0$. The model does not have an active ice component and the ice is not advected by the ocean. We assume that the ice distribution is a steady balance between wind stress, ocean stress, internal ice stresses, and formation/melt from interactions with the atmosphere and ocean. This is justified by the observation that ice is present near Greenland at all times and, over long space and time scales, follows a general pattern of increasing ice thickness in the direction of Greenland. A simple model for the ice thickness in the central Arctic demonstrates such a steady balance (Spall 2019).

For the central calculation, the model was run for a period of 40 years with mean fields calculated over the final 15 years of integration. The bottom drag coefficient $C_d = 0.0012\ m\ s^{-1}$ and the ice-ocean drag coefficient is $C_i = 1 \times 10^{-4}\ m\ s^{-1}$. The nondimensional Smagorinsky Laplacian coefficient $\nu_s = 2.5$. The primary sensitivity to these choices is that the gyres become more unstable for lower values of C_i, resulting in weaker mean gyres (Meneghello et al. 2020).

b. Model results

We present results from 4 model simulations. The first is a case with sea ice with the ice-ocean drag term but with no ice pumping. The impact of the pumping is then demonstrated by including the right hand side term in (9). The overall impact of ice is shown by removing both the ice-ocean drag term and the ice pumping term. Finally, we repeat the ice pumping calculation in which the ice thickness keeps the same pattern but its amplitude oscillates in time with $\phi = 1$ in (12).

The mean upper layer streamfunction for the case with ice-ocean drag but no ice pumping is shown in Fig.6a. The maximum transport in the anticyclonic gyre is about 6 Sv, while that in the cyclonic gyre is about -3.5 Sv. The smaller transport in the cyclonic gyre results from the thinner upper layer, an asymmetry not included in quasigeostrophic dynamics. The upper layer thickness varies from about 350 m in the anticyclonic gyre to 65 m in the cyclonic gyre. The velocity in the region between the thick upper layer and the thin upper layer is $O(5\ \mathrm{cm\ s^{-1}})$.

The case with ice pumping produces a stronger anticyclonic gyre (6.8 Sv) and a weaker cyclonic gyre (-2.4 Sv), Fig. 6b. The pathway of the model Transpolar Drift Current is also shifted towards the cyclonic gyre. Taking the difference between b) and a) shows that the ice pumping produces a basin-scale anticyclonic circulation anomaly, centered at the pole, of magnitude 3.5 Sv. This is consistent with the circulation pattern and strength predicted by the theory in the previous section[1]. The upper layer thickness reflects this anticyclonic circulation such that the halocline is deeper near the pole and shallower around the basin perimeter. The halocline is adiabatic in this model so this change in layer thickness integrates to zero over the basin.

Sea ice acts to stabilize the gyres due to the ice-ocean drag term (Meneghello et al. 2021). This is reflected by the case with no sea ice shown in Fig. 7b, where the anti-

[1]Keep in mind that the model and theory have different patterns of surface stress.

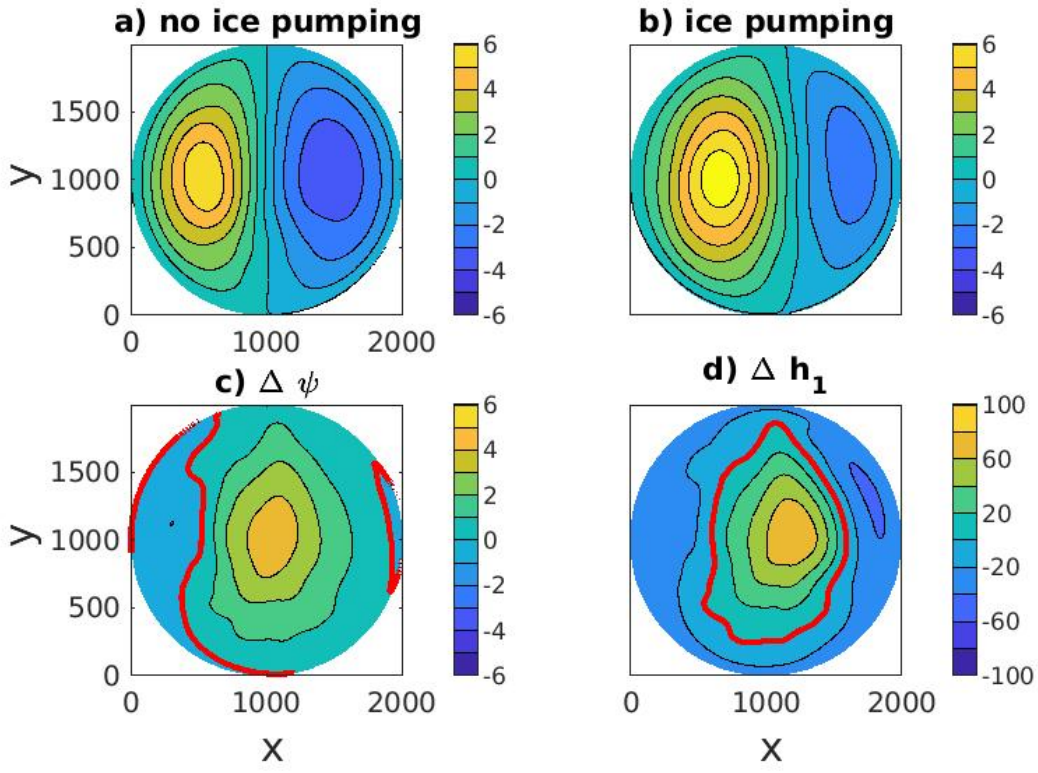

FIG. 6: a) Upper layer streamfunction (Sv) for the case with ice-ocean drag but a) no ice pumping b) with ice pumping. The difference between the case with ice pumping relative to the case without ice pumping for the upper layer c) streamfunction (Sv), d) thickness (m). The red line in c) and d) is the zero contour.

cyclonic gyre is only 4.3 Sv and the cyclonic gyre is -3.1 Sv. This is accompanied by a shallower halocline in the central and anticyclonic basin and a deeper halocline in the cyclonic basin.

The ice cover in the Arctic Ocean has a strong seasonal cycle. This is approximated here by setting $\phi = 1$ in (12). This reduces the mean ice thickness, and ice cover slope, by a factor of 2. This results in no ice gradient, or pumping, during the model summer, although in reality there is an ice cover slope present north of Greenland all year long. The purpose of this calculation is to test whether the ice-ocean coupling is approximately linear in this parameter regime so that the influences of sea ice can be approximated by the annual mean ice distribution. The time mean streamfunction shows the same pattern of anomalous circulation compared to the case with no ice pumping, just reduced by a factor of 2 (Fig. 8). So we can expect that the basic mechanism demonstrated by these steady solutions will be found even in the presence of a strong seasonal cycle. In addition, there is a rapid, barotropic response to the varying ice thickness gradient such that the anomalous anticyclonic gyre spins up and down on the seasonal time scale with an amplitude of $O(1$ Sv).

4. Discussion and conclusion

The sloping sea-ice cover acts as an upside-down bathymetry, generating a vertical velocity, which we dub ice pumping, and steering the underlying circulation in a manner comparable to bottom topography. Our observational estimates (Figure 2) suggest that the ice pumping influence on the large-scale circulation dynamical balance is, in the central Arctic, comparable to that of mesoscale eddies and of planetary vorticity advection. Our theoretical and numerical models show how small ice-thickness gradients, of the order of a meter over a 1000 km, combined with mean surface currents of a few centimeters per second are sufficient to generate an ice pumping driving a substantial change in the large-scale circulation.

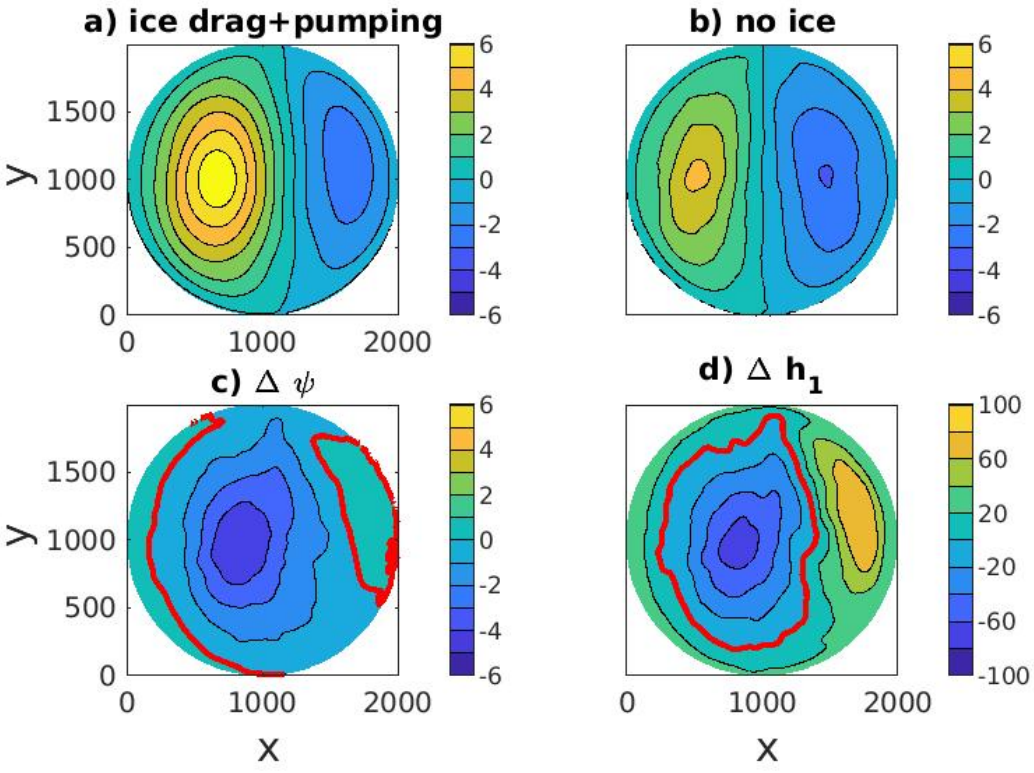

FIG. 7: a) Upper layer streamfunction (Sv) for the case with ice-ocean drag and ice pumping b) no sea ice. The difference between the case with ice and the case without ice for the upper layer c) streamfunction (Sv), d) thickness (m). The red line in c) and d) is the zero contour.

Crucially, the ice-pumping mechanism remains dynamically relevant even on the long time scales for which the deep circulation is typically assumed to be at rest and classical topographic steering is therefore expected to play only a minor role away from the coast. This is particularly important given that the Arctic wind-driven circulation is largely confined to the upper 300 m, whereas most bathymetry outside the continental shelves lies deeper than 2000 m. We therefore propose that ice thickness needs to be considered in a conservation principle analogous to f/h in an ice-free ocean, in which h is set by ice thickness in addition to bathymetry, especially on long time scales.

Our analyses capture the main features of the Arctic circulation, but remain idealized. Nonetheless, some general conclusions about the impact of ice pumping on the Arctic circulation are robust across the theory and the numerical model, and can be put forth. These are summarized in Figure 9. As the ice thickness gradient is varied from zero ($\mathsf{P} = 0$) to 2 m every 1000 km ($\mathsf{P} = 2$), the Transpolar Drift Current — marked by the streamline separating the anticyclonic and the cyclonic gyre — and the center of the two gyres — marked by dots — shift rightward toward the Eurasian coast. The current's outflow moves eastward by more than 500 km, possibly redirecting a larger fraction of the transport towards the Greenland Current and outside the Arctic (not represented in our model) rather than towards the recirculating Beaufort gyre (Figure 9a and 9c).

Shifts in the Transpolar Drift Current are accompanied by changes in gyre transport. As the ice thickness gradient increases, the anticyclonic gyre grows in size and the cyclonic gyre weakens, as shown in Figure 9d. The ratio of the two gyres transports, $\frac{\min(\tilde{h})-h_b}{\max(\tilde{h})-h_b}$, where h_b is the layer thickness at the transpolar drift (the same as at the boundary), is presented in Figure 9b as a function of the ice-pumping strength P and the combined governor/eddy-flux parameter $\alpha\mathsf{G}+\mathsf{K}$. The circulations at the extremes of parameter space the ones shown in Figure 4: the circulation at the origin (panel a), the symmetric circulation for

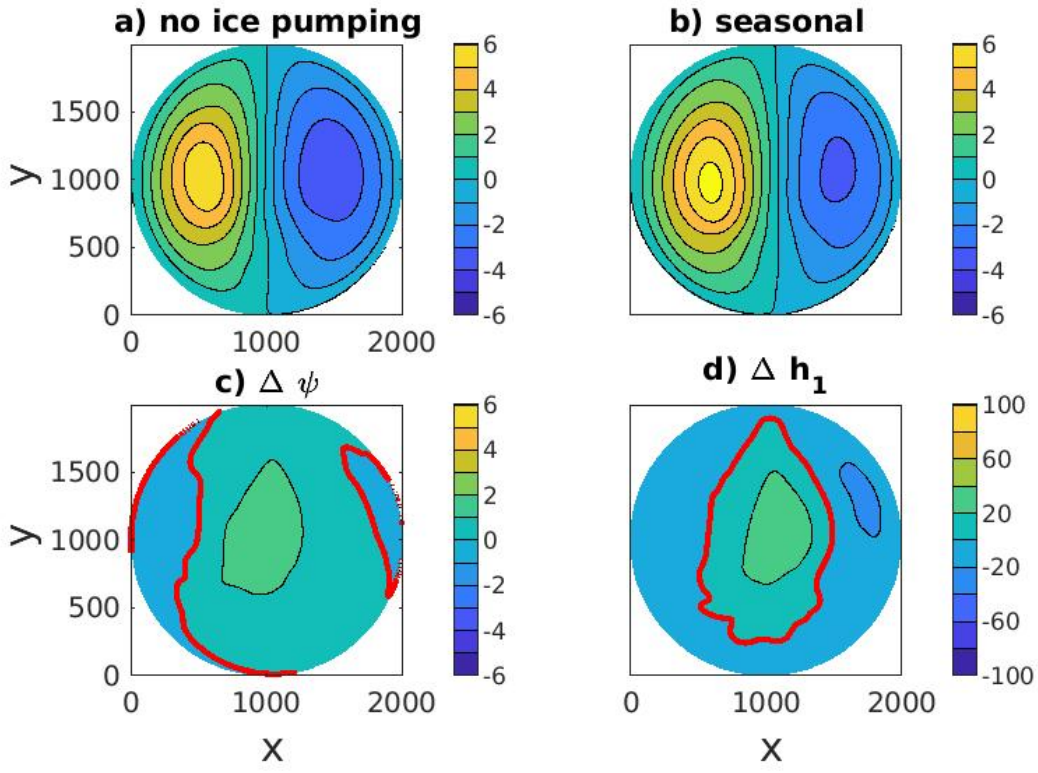

FIG. 8: Upper layer streamfunction (Sv) for a) the central case with ice-ocean drag and ice pumping b) a seasonal cycle. The difference between the case without and with c) streamfunction (Sv), d) thickness (m). The red line in c) and d) is the zero contour.

large $\alpha\mathsf{G}+\mathsf{K}$ (panel b), and the single-gyre circulation for large P (panel c). The circulation for comparable P and $\alpha\mathsf{G}+\mathsf{K}$ is the one shown in Figure 5b.

Our study focuses on the Arctic, but the theory developed here is sufficiently general to apply to other ice-covered oceans. A candidate application are oceans on icy moons such as Enceladus and Europa, where ice-thickness gradients are much larger than in the Arctic and current speeds may be comparable. For example, Enceladus exhibits sea-ice thickness variations of order 10 km over characteristic length scales of about 100 km, corresponding to ice-thickness gradients roughly 10^5 times larger than those on Earth (Čadek et al. 2016), while ocean currents are estimated to be on the order of centimeters per second (Soderlund 2019). In such environments, the Ekman pumping term would need to be replaced by an alternative source of potential vorticity. Nevertheless, the remainder of the theoretical framework is expected to remain applicable, and the large ice-thickness gradients suggest that ice pumping may play an important dynamical role.

Acknowledgments. GM acknowledges support by the ANR program under grant ANR-22-CPJ2-0063-01. MAS was supported by NSF Grants OCE2241083 and OCE2420209.

Data availability statement. The observational datasets used in this estimate are: sea-ice thickness from Ricker et al. (2017); sea-ice concentration from Meier et al. (2024); sea-ice velocity from Tschudi et al. (2019); dynamic ocean topography from Armitage et al. (2016, 2017); and geostrophic winds derived from atmospheric geopotential fields from Hersbach et al. (2023).

References

Armitage, T. W. K., S. Bacon, A. L. Ridout, A. A. Petty, S. Wolbach, and M. Tsamados, 2017: Arctic Ocean surface geostrophic circulation 2003–2014. *The Cryosphere*, **11 (4)**, 1767–1780, https://doi.org/10.5194/tc-11-1767-2017.

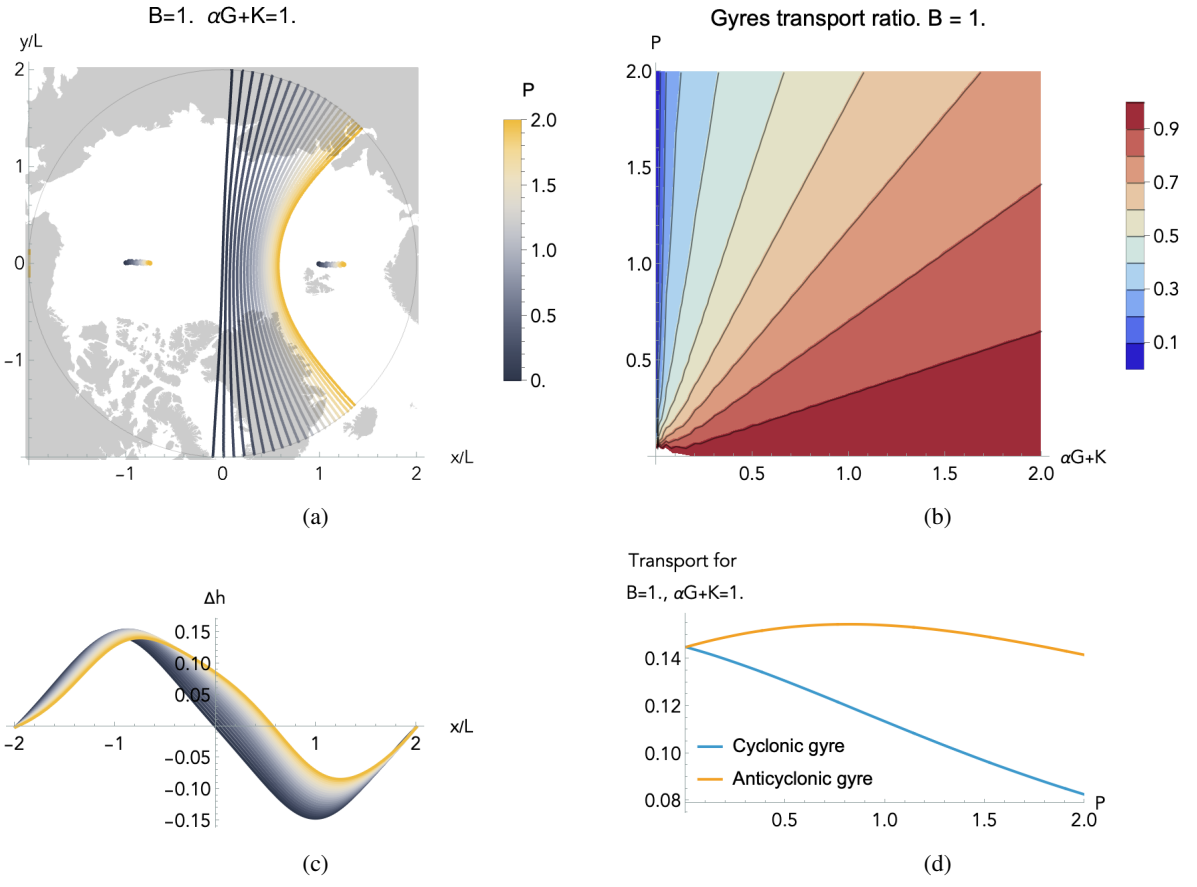

FIG. 9: Modulation of Arctic circulation by ice pumping. (a) The Transpolar Drift Current trajectory (lines) and the gyres' center (points) as a function of the ice pumping parameter P (color), overlaid on a map of the Arctic; (b) the ratio between the cyclonic and the anticyclonic gyres' transport, as a function of the ice pumping parameter P and the governor/thickness diffusion parameter $\alpha\mathsf{G}+\mathsf{K}$; (c) isopycnal depth anomaly along the line connecting the gyres centers, as a function of the ice pumping parameter P; (d) the gyres transport for $\alpha\mathsf{G}+\mathsf{K}=1$ as a function of P. As the ice thickness increases, the Transpolar Drift Current trajectory and the gyre centers moves towards the Eurasian coast, and the cyclonic gyre's transport is reduced.

Armitage, T. W. K., S. Bacon, A. L. Ridout, S. F. Thomas, Y. Aksenov, and D. J. Wingham, 2016: Arctic sea surface height variability and change from satellite radar altimetry and GRACE, 2003-2014. *Journal of Geophysical Research: Oceans*, **121 (6)**, 4303–4322, https://doi.org/10.1002/2015JC011579.

Davis, P. E. D., C. Lique, and H. L. Johnson, 2014: On the Link between Arctic Sea Ice Decline and the Freshwater Content of the Beaufort Gyre: Insights from a Simple Process Model. *J. Phys. Oceanogr.*, **33**, 8170–8184.

Dewey, S., J. Morison, R. Kwok, S. Dickinson, D. Morison, and R. Andersen, 2018: Arctic Ice-Ocean Coupling and Gyre Equilibration Observed With Remote Sensing. *GEOPHYSICAL RESEARCH LETTERS*, **45 (3)**, 1499–1508, https://doi.org/10.1002/2017GL076229.

Doddridge, E. W., G. Meneghello, J. Marshall, J. Scott, and C. Lique, 2019: A three-way balance in the Beaufort Gyre: The ice-ocean governor, wind stress, and eddy diffusivity. *J. Geophys. Res.*, **124**, 3107–3124, https://doi.org/10.1029/2018/JC014897.

Hersbach, H., and Coauthors, 2023: Era5 post-processed daily statistics on pressure levels from 1940 to present. Copernicus Climate Change Service (C3S) Climate Data Store (CDS), URL https://cds.climate.copernicus.eu, https://doi.org/10.24381/cds.4991cf48.

Lique, C., H. L. Johnson, and P. E. D. Davis, 2015: On the Interplay between the Circulation in the Surface and the Intermediate Layers of the Arctic Ocean. *J. Phys. Oceanogr.*, **45**, 1393 1409, https://doi.org/https://doi.org/10.1175/JPO-D-14-0183.1.

Manucharyan, G., and M. A. Spall, 2015: Wind-driven freshwater buildup and release in the Beaufort Gyre constrained by mesoscale eddies. *Geophys. Res. Lett.*, **42**, https://doi.org/doi:10.1002/2015GL065957.

Meier, W., F. Fetterer, A. Windnagel, J. S. Stewart, and T. Stafford, 2024: Noaa/nsidc climate data record of passive microwave sea ice concentration, version 5. National Snow and Ice Data Center, URL https://nsidc.org/data/g02202/versions/5/, https://doi.org/10.7265/RJZB-PF78.

Meneghello, G., E. Doddridge, J. Marshall, J. Scott, and J. M. Campin, 2021: Genesis and decay of mesoscale baroclinic eddies in the seasonally ice-covered interior arctic ocean. *J. Phys. Oceanogr.*, https://doi.org/doi:10.1175/JPO-D-20-0054.1.

Meneghello, G., J. Marshall, J.-M. Campin, E. Doddridge, and M.-L. Timmermans, 2018a: The Ice-Ocean Governor: Ice-Ocean Stress Feedback Limits Beaufort Gyre Spin-Up. *Geophys. Res. Lett.*, **45**, 11 293–11 299, https://doi.org/https://doi.org/10.1029/2018GL080171.

Meneghello, G., J. Marshall, S. T. Cole, and M.-L. Timmermans, 2017: Observational Inferences of Lateral Eddy Diffusivity in the Halocline of the Beaufort Gyre. *Geophys. Res. Lett.*, **44**, 12 331–12 338, https://doi.org/10.1002/2017/GL075126.

Meneghello, G., J. Marshall, C. Lique, P. Isachsen, E. Doddridge, J.-M. Campin, H. Regan, and C. Talandier, 2020: Exploring the role of the "ice-ocean governor" and mesoscale eddies in the equilibration of the Beaufort Gyre: Lessons from observations. *J. Phys. Oceanogr.*, **50**, https://doi.org/doi:10.1175/JPO-D-20-0054.1.

Meneghello, G., J. Marshall, M.-L. Timmermans, and J. Scott, 2018b: Observations of Seasonal Upwelling and Downwelling in the Beaufort Sea Mediated by Sea Ice. *J. Phys. Oceanogr.*, **48**, 795–805.

Munk, W. H., 1950: On the wind-driven ocean circulation. *Journal of Atmospheric Sciences*, **7 (2)**, 80 – 93, https://doi.org/10.1175/1520-0469(1950)007⟨0080:OTWDOC⟩2.0.CO;2, URL https://journals.ametsoc.org/view/journals/atsc/7/2/1520-0469_1950_007_0080_otwdoc_2_0_co_2.xml.

Nilsson, J., J.-A. H. Kallmyr, and P. E. Isachsen, 2024: Topographic Steering of the Upper Arctic Ocean Circulation by Deep Flows. *Tellus*, **76**, 206–226, https://doi.org/DOI:10.16993/tellusa.4072.

Nöst, O. A., and P. E. Isachsen, 2003: The large-scale time-mean ocean circulation in the Nordic Seas and Arctic Ocean estiamted from simplified dynamics. *J. Mar. Res.*, **61**, 175–210.

Ricker, R., S. Hendricks, L. Kaleschke, X. Tian-Kunze, J. King, and C. Haas, 2017: A weekly Arctic sea-ice thickness data record from merged CryoSat-2 and SMOS satellite data. *Cryosphere*, **11 (4)**, 1607–1623, https://doi.org/10.5194/tc-11-1607-2017.

Smagorinsky, J., 1963: General circulation experiments with the primitive equations:I. The basic experiment. *Mom. Wea. Rev.*, **91**, 99–164.

Soderlund, K. M., 2019: Ocean dynamics of outer solar system satellites. *Geophysical Research Letters*, **46 (15)**, 8700–8710, https://doi.org/https://doi.org/10.1029/2018GL081880, URL https://agupubs.onlinelibrary.wiley.com/doi/abs/10.1029/2018GL081880, https://agupubs.onlinelibrary.wiley.com/doi/pdf/10.1029/2018GL081880.

Spall, M. A., 2019: Dynamics and thermodynamics of the mean Transpolar Drift and ice thickness in the Arctic Ocean. *J. Climate*, **32**, 8449–8463, https://doi.org/10.1175/JCLI-D-19-0252.1.

Spall, M. A., 2020: Potential vorticity dynamics of the Arctic halaocline. *J. Phys. Oceanogr.*, **50**, 2491–2506, https://doi.org/DOI:10.1175/JPO-D-20-0056.1.

Sverdrup, H. U., 1947: Wind-driven currents in a baroclinic ocean; with application to the equatorial currents of the eastern pacific*. *Proceedings of the National Academy of Sciences*, **33 (11)**, 318–326, https://doi.org/10.1073/pnas.33.11.318, URL https://www.pnas.org/doi/abs/10.1073/pnas.33.11.318, https://www.pnas.org/doi/pdf/10.1073/pnas.33.11.318.

Tschudi, M., W. N. Meier, J. S. Stewart, C. Fowler, and J. Maslanik, 2019: Polar Pathfinder Daily 25 km EASE-Grid Sea Ice Motion Vectors, Version 4. Tech. rep., NASA National Snow and Ice Data Center Distributed Active Archive Center, Boulder, Colorado USA. https://doi.org/10.5067/INAWUWO7QH7B.

Willmott, A. J., and M. Luneva, 2015: Steady, barotropic wind and boundary-driven circulation on a polar plane. *Geophys. Astrophys. Fluid Dyn.*, **109**, 216–233, https://doi.org/10.1080/03091929.2015.1050589.

Yang, J., A. Proshutinsky, and X. Lin, 2016: Dynamics of an idealized Beaufort Gyre: 1. The effect of a small beta and lack of western boundaries. *J. Geophys. Res.*, **121**, 1249–1261, https://doi.org/10.1002/2015JC011296.

Zhong, W., M. Steele, J. Zhang, and J. Zhao, 2018: Greater Role of Geostrophic Currents in Ekman Dynamics in the Western Arctic Ocean as a Mechanism for Beaufort Gyre Stabilization. *Journal of Geophysical Research: Oceans*, **123 (1)**, 149–165, https://doi.org/10.1002/2017JC013282, URL http://doi.wiley.com/10.1002/2017JC013282.

Čadek, O., and Coauthors, 2016: Enceladus's internal ocean and ice shell constrained from cassini gravity, shape, and libration data. *Geophysical Research Letters*, **43 (11)**, 5653–5660, https://doi.org/https://doi.org/10.1002/2016GL068634, URL https://agupubs.onlinelibrary.wiley.com/doi/abs/10.1002/2016GL068634, https://agupubs.onlinelibrary.wiley.com/doi/pdf/10.1002/2016GL068634.